

MULTI-OBJECTIVE OPTIMIZATION OF AERO-ENGINE BEARING CHAMBER SCAVENGE STRUCTURE BASED ON NSGA-II

Zetao ZHU , Yaguo LYU*, Le JIANG, Zhenxia LIU, Shu LI, Fulin LIU
School of Power and Energy, Northwestern Polytechnical University, Xi'an, China

Abstract

Driven by the demand for improved performance, aero-engine bearing chambers must achieve both efficient oil circulation and effective wall heat transfer under increasingly severe operating conditions. Existing designs typically consider oil scavenging and heat transfer processes separately, and a comprehensive optimization framework that enhances both aspects remains lacking. To address this issue, this study investigates the oil scavenging and heat transfer characteristics of a novel offset scavenge bearing chamber, and conducts structural optimization using the NSGA-II method. The results show that the offset scavenge structure improves oil evacuation through oil guidance, while the reduced wall oil film coverage results in a lower wall-averaged Nusselt number. Increasing rotational speed decreases oil scavenging efficiency but raises the Nusselt number. A higher oil supply rate enhances both oil scavenging and wall heat transfer performance, whereas a higher oil supply temperature degrades both. After optimization, the offset scavenge bearing chamber achieves a 7.96% increase in oil scavenging efficiency and a 4.22% increase in the Nusselt number. These findings provide valuable insights for refined lubrication system design and thermal management optimization in aero-engines.

Keywords: Bearing chamber; Oil scavenging performance; Thermal management; Two-phase flow; Multi-objective optimization

1. Introduction

In the global pursuit of carbon neutrality[1], advancing green and low-carbon aviation engine technologies is essential for achieving sustainable development in the aviation industry and addressing the challenges posed by climate change[2]. With trends toward increasing engine output power, turbine inlet temperature, and other parameters, main shaft bearings must operate reliably under complex conditions involving high temperatures, rotational speeds, and heavy loads. As a bearing housing integrated with lubrication and sealing systems, the bearing chamber supports load transmission and facilitates lubrication, cooling, oil-air recovery, and sealing isolation, making it a core functional unit of the lubrication system[3].

During engine operation, oil dispersed into the bearing chamber interacts with the air inside, creating a two-phase flow. From a performance perspective, the supplied oil should be promptly scavenged to remove heat from the chamber. However, strong airflow shear promotes recirculating oil-air motion, causing some oil to escape through the vent and resulting in oil loss[4]. Additionally, a decrease in scavenging capability leads to prolonged oil retention within the chamber, increasing the

https://doi.org/10.71945/icas2026_0623

risks of overheating, coking, and potential oil combustion[5]. Therefore, achieving efficient oil scavenging in the bearing chamber is a critical challenge to ensure the reliability of the entire engine and flight safety.

The strong coupling between heat and mass transfer within the chamber arises from the combined effects of multiple boundary conditions. The air-phase flow directly influences droplet transport and oil film behavior through shear effects. Lee et al.[6] analyzed the airflow and the effects of shafts rotation. Aidarinis et al.[7] measured the flow characteristics of sealing air in the bearing chamber under various rotational speeds, mass flow rates, and geometric configurations, and effectively simulated the airflow through the bearing region using a porous medium model. Glahn et al.[8] developed a droplet motion simulation model based on an Euler–particle approach coupled with a spray model, enabling the prediction of droplet trajectories and velocities, and quantitatively analyzed the effects of droplet size, impact angle, and impact velocity on coalescence and breakup behavior[9]. Farrall et al.[10] developed a criterion to predict droplet impacts on chamber walls and determined the motion trajectories of droplets originating from the bearing. Zhu et al.[11] developed a theoretical model that accounts for droplet physical process, and determined the sizes and motion parameters of droplets detached from oil films. Singh et al.[12] proposed an enhanced Eulerian oil-film model that incorporates additional shear forces due to contact angles, successfully reproducing the phenomenon of partial wall-film spreading at low oil-film flow rates, consistent with experimental observations.

Simmons et al.[13] demonstrated that two-way coupled models more accurately capture air-oil interactions, particularly emphasizing that small droplets are highly sensitive to changes in airflow. Young et al.[14] employed the Volume of Fluid (VOF) method to calculate the oil-air flow. Kirov et al.[15] compared various two-phase flow computational methods for predicting two-phase flow patterns. Although the Euler multiphase diffusion model incurs higher computational costs, it captures nearly all liquid motion within the chamber, whereas the Eulerian oil-film model provides relatively accurate results only at the scavenge outlet. Kurz et al.[16] identified rotor speed as the dominant parameter controlling oil-film flow behavior and proposed a composite parameter for predicting flow regime transitions, establishing a foundation for correlating flow patterns with wall heat transfer.

The oil–air medium flow governs the transport processes of energy generation and transfer. Previous studies have demonstrated that operating parameters significantly affect the heat transfer coefficient[17] and temperature distribution[18]. Building on this foundation, subsequent modeling studies have further indicated that the oil film flow regime and its thickness are key factors governing local wall heat transfer[19]. Additionally, heat transfer correlations have been refined and extended by incorporating the effects of chamber geometry[20]. Petukhov et al.[21] proposed a method to estimate the convective heat transfer coefficient at chamber walls using heterogeneous medium mechanics, deriving a two-dimensional Lagrangian model through axial averaging. Tatar et al.[22] compared two empirical heat-transfer models for bearing chambers and found that models incorporating Reynolds numbers related to both oil and seal air provide better predictions of wall temperatures.

With the continuous advancement in understanding physical processes, enhancing the operational performance of bearing chambers through parameter regulation and structural optimization has become a primary research focus. The first approach involves modifying the scavenge structure by altering the external chamber geometry. Chandra et al.[23] found that the flow regime within the bearing chamber transitions between gravity-dominated and shear-dominated mechanisms as shaft speed varies, and that the oil ejection process is strongly influenced by chamber geometry and operating conditions[24]. Building on this, they experimentally investigated the scavenge performance of bearing chambers with deep-groove structures, determining the liquid-phase retention volumes under

various flow rates and rotational speeds[25]. The second approach aims to improve scavenge performance without changing the external profile by incorporating internal attachments or inserts. Adeniyi et al.[26] numerically optimized a grille-type insert to improve oil retention and enhance scavenge efficiency within the bearing chamber. Kurz et al.[27] measured oil-film thicknesses in scavenge structures with and without cover plates, finding that deep-groove structures with cover plates achieved higher scavenge efficiency, and that oil-film thickness at high rotational speeds was significantly lower than in conventional structures. Furthermore, machine learning and multi-objective optimization methods have been increasingly applied in aero-engine design, including compressor aerodynamic force prediction[28], compressor flow-field reconstruction[29], film-cooling prediction[30], and turbomachinery seal-cavity optimization[31].

In summary, although significant progress has been made in two-phase flow, wall heat transfer, and scavenge structure design within bearing chambers, most existing studies have treated oil flow and heat transfer separately. The influence of scavenge structure modifications on their coupled performance remains insufficiently clarified, and an optimization framework that simultaneously considers oil scavenging efficiency and wall heat transfer performance is still lacking. To address this gap, this study introduces an innovative bearing chamber featuring an offset scavenge structure. Its effects on oil scavenging and heat transfer performance are investigated through comparison with a conventional design. Building on this, a multi-objective optimization framework based on the Non-dominated Sorting Genetic Algorithm II (NSGA-II) is established to optimize the offset oil scavenging structure.

2. Methods

2.1 Chamber configuration and computational mesh

Figure 1 shows the rear turbine support bearing chamber in an aero-engine. Two bearings within the chamber support the high-pressure (HP) and low-pressure (LP) rotors, respectively. The scavenge outlet is located vertically at the bottom of the chamber, while a vent at the top maintains pressure balance. Sealing structures are positioned on both sides of the chamber and between the shafts to prevent oil leakage. During engine operation, lubricating oil is thrown into the chamber through the bearings (indicated by red arrows) and interacts with leakage air (indicated by blue arrows), forming a two-phase flow. Simultaneously, heat is exchanged with the high-temperature chamber wall.

Figure 2 shows the computational model of the conventional bearing chamber. Since the influence of the bearing geometry on the oil throw-off velocity is negligible, the bearing components were omitted from the model, and the oil and air inlets were simplified as annular planes[32]. The computational model includes the HP and LP rotors, sealing air inlets, bearing chamber walls, vent outlet, and scavenge outlet. Both the HP and LP shafts rotate clockwise around the x-axis.

Based on this design, a novel offset-scavenge bearing chamber was developed, as illustrated in Figure 3. By incorporating a scavenge groove and adopting a curved transition with a tangential ramp configuration, the structure forms a continuous connection with the chamber inner wall, thereby guiding the oil scavenging process. The main structural parameters of the offset-scavenge bearing chamber include a vent diameter (d_v) of 11.5 mm, a scavenge outlet diameter (d_s) of 11.5 mm, an offset distance (w) of 35.0 mm, and a scavenge groove depth (h) of 25.0 mm. The vent and scavenge outlet dimensions of the conventional bearing chamber are kept consistent with those of the side-opening configuration to ensure that flow differences among the various configurations are caused solely by the scavenge outlet arrangement.

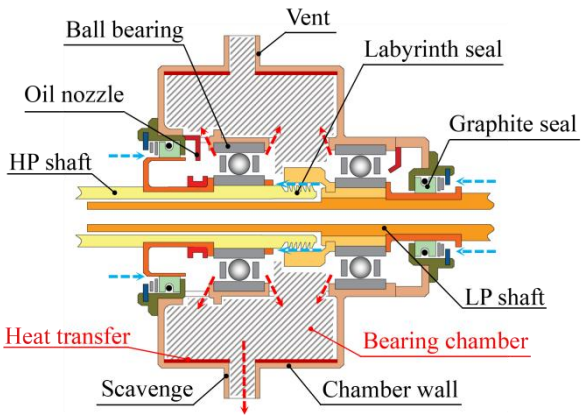


Figure 1–Turbine aft support bearing chamber

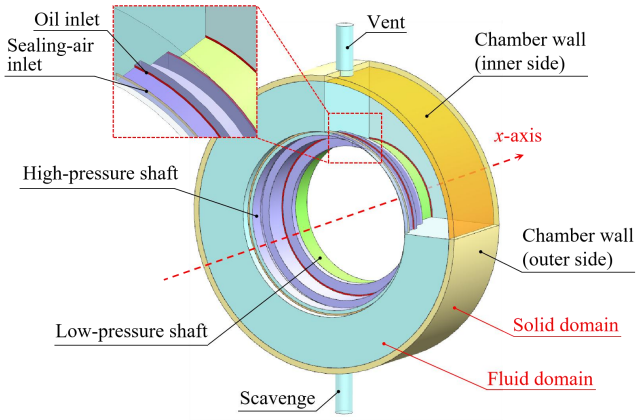
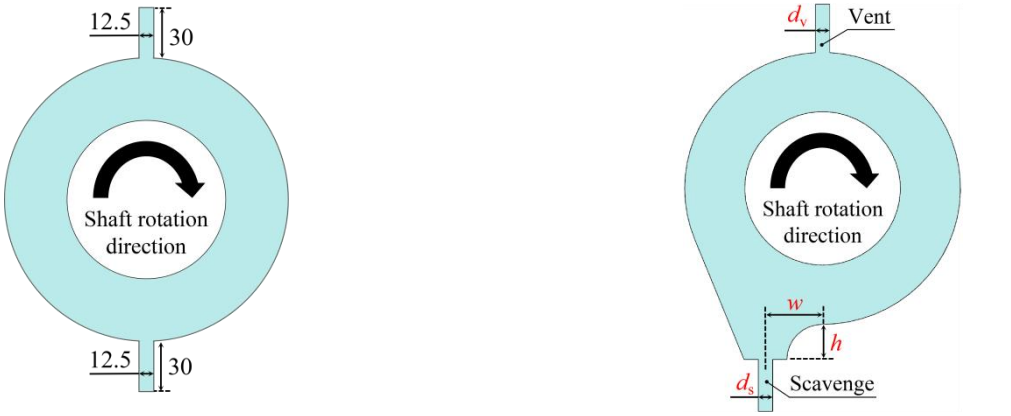


Figure 2–Computational model



(a) Conventional design (b) Offset-scavenge design

Figure 3–Different oil scavenge port configurations

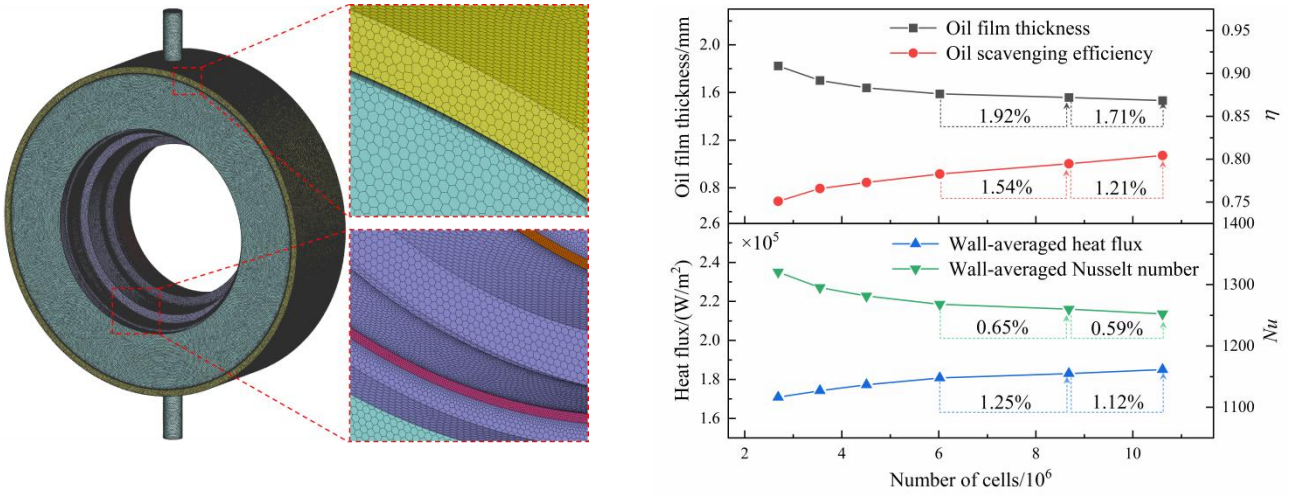
2.2 Boundary conditions and parameter definitions

The computational domain of the conventional bearing chamber was discretized using polyhedral meshes. As shown in Figure 4(a), the basic mesh size in the main flow region was approximately 0.88 mm. Local mesh refinement was applied near the oil inlet, air inlet, vent outlet, and scavenge outlet, with a minimum mesh size of 0.12 mm. Twelve prism layers were generated near the wall, with the first layer thickness set to 0.012 mm and a growth rate of 1.1. The near-wall y^+ value was approximately 1.2, meeting the requirements of the turbulence model.

To verify mesh independence, six mesh schemes were generated with cell counts of 2.69×10^6, 3.55×10^6, 4.51×10^6, 6.02×10^6, 8.68×10^6, and 10.61×10^6. Oil film thickness and oil scavenging efficiency were selected as flow indicators, while wall-averaged heat flux and wall-averaged Nusselt number served as heat transfer indicators. As shown in Figure 4(b), all indicators gradually stabilized as the cell count increased. When the cell count increased from 8.68×10^6 to 10.61×10^6, the relative variations in oil film thickness, oil scavenging efficiency, wall-averaged heat flux, and wall-averaged Nusselt number were 1.71%, 1.21%, 1.12%, and 0.59%, respectively. Considering both computational accuracy and cost, the mesh scheme with 8.68×10^6 cells was adopted for the subsequent simulations.

The walls of the HP and LP rotating shafts were defined as moving walls. The oil and air inlets were specified as mass-flow inlets, while both the scavenge and vent outlets were designated as pressure outlets. The gauge pressure at the outlets was set to 0 Pa, and the operating pressure was set to 101325 Pa. The operating parameters of the bearing chamber included the HP shaft speed (n), oil supply flow rate (q_{oil}), oil supply temperature (T_{oil}). Under design-point conditions, the high-pressure

rotor speed was 16000 r/min, the low-pressure rotor speed was 11000 r/min, the oil supply temperature was 423.15 K, and the total oil supply flow rate was 4 L/min, evenly distributed between the two bearings. The sealing air flow rate was set at 1.5 g/s based on the bleed air capacity of the air system and the sealing pressure difference, with a sealing air temperature of 423.15 K.



(a) Computational mesh (b) Verification results

Figure 4–Mesh independence verification

The parameter ranges used to investigate the effects on oil scavenging performance are listed in Table 1. The HP shaft speed varied from 75% to 125% of the design-point value. Since the oil flow inside the bearing chamber is primarily driven by the HP rotor, the LP shaft speed was fixed at 11000 r/min to reduce the number of variables and highlight the influence of the high-pressure shaft speed. Mobil Jet Oil II was used as the lubricating oil. The ranges of the structural parameters were established according to geometric constraints. The offset distance varied from 1/8 to 1/3 of the outer diameter. The curved surface radius covered the deep-groove and shallow-groove ranges defined by Adeniyi et al.[26]. The vent and scavenge outlet diameters were specified according to the characteristics of the upstream and downstream components of the lubrication system.

Table 1 Parameter ranges

Parameters	Value range
n/(r/min)	12000–20000
q_{oil}/(L/min)	2–6
T_{oil}/K	323.15–423.15
w/mm	24–64
h/mm	15–35
d_v/mm	10–18
d_s/mm	10–18

To quantify the overall flow and heat transfer performance, the scavenge efficiency (η) and wall Nusselt number (Nu) were used to evaluate oil evacuation and wall heat transfer, respectively. The scavenge efficiency is defined as follows:

$$\eta = \frac{m_{i,s}}{m_{oil}} = \frac{\int_{t_1}^{t_2} \dot{m}_{i,s} \mathrm{d}t}{\rho_{oil} q_{oil} (t_2 - t_1)} \tag{1}$$

where $m_{i,s}$ and m_{oil} are the oil mass discharged through the scavenge outlet and the total supplied oil mass during the time interval, respectively. The selected time interval was located within the

statistically stable stage of the transient simulation. ρ_{oil} and q_{oil} denote the oil density and volumetric oil supply flow rate, respectively.

The heat transfer process in the bearing chamber was modeled as a conjugate heat transfer problem. Heat transfer occurs via convection within the fluid domain and conduction through the solid wall. The wall material was assumed to be isotropic, and thermal contact resistance at the fluid-solid interface was neglected. The wall heat transfer performance was characterized by the Nusselt number:

$$Nu = \frac{\overline{h_c} D_h}{\lambda_{oil}} \tag{2}$$

$$\overline{h_c} = \frac{1}{A}\int_A h_c \mathrm{d}A \tag{3}$$

where D_h is the hydraulic diameter, selected as the characteristic length:

$$D_h = \frac{2bs}{b+s} \tag{4}$$

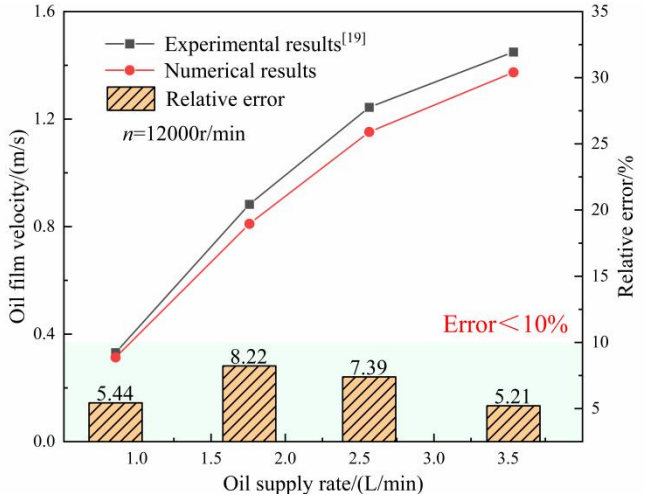
where b is the chamber length and s is the difference between the outer and inner diameters.

2.3 Numerical solution and method validation

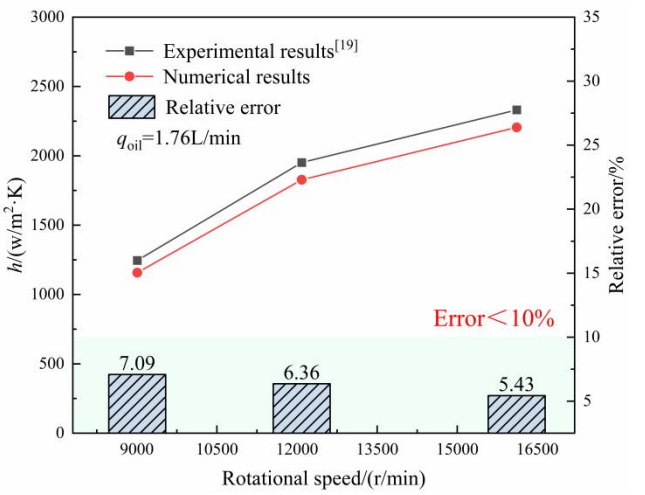
The Volume of Fluid (VOF) method[33] was employed to simulate the two-phase flow within the bearing chamber. The phase interface was tracked by solving the volume fraction transport equation, while the energy equation was solved throughout the entire computational domain. The thermophysical properties of the mixture were determined using a volume-fraction-weighted formulation. The Shear Stress Transport (SST) k-ω model[34] was employed to describe turbulent flow, due to its strong performance in predicting near-wall shear and boundary layer development. Simulations were conducted using ANSYS Fluent. The transient term was discretized with a first-order implicit scheme, while pressure interpolation was handled using the PRESTO! scheme. The momentum, energy, and turbulence equations were discretized using a second-order upwind scheme. The air-oil interface was reconstructed using the Geo-Reconstruction scheme, and surface tension was modeled via the Continuum Surface Force (CSF) method.

The solution was considered converged when the residuals of all variables were below 1×10^{-6}. The simulation was regarded as statistically stable when the oil mass imbalance between the inlet and outlet was less than 1%, and the wall temperature and heat flux showed stable temporal variations. The global Courant number was maintained between 0.8 and 1.2, and the time step was adjusted between 2×10^{-5} s and 5×10^{-5} s.

The numerical method was validated using experimental data from a rotating bearing chamber test rig[19]. Oil film velocity and convective heat transfer coefficient were chosen as validation metrics for flow and heat transfer, respectively. The film velocity was measured at 30° downstream of the scavenge outlet, consistent with the experimental measurement location. After the flow reached a statistically steady state, time-averaged values over 1 s were used for comparison. Figure 5 presents the validation results for oil supply and sealing air temperatures of 150 °C, with a sealing air flow rate of 10 g/s. As shown in Figure 5(a), the predicted oil film velocity closely matches the experimental data, exhibiting an average relative error of 6.57%. Figure 5(b) compares the convective heat transfer coefficient at different rotational speeds, with an average relative error of 6.29%. All relative errors are below 10%, indicating that the numerical method can reliably predict the two-phase flow and wall heat transfer characteristics within the rotating cavity. Therefore, the current model is deemed suitable for the subsequent analysis of oil scavenging and heat transfer performance.



(a) Flow validation



(b) Heat transfer validation

Figure 5–Validation of the numerical method

2.4 Multi-objective optimization framework

A general multi-objective optimization problem can be expressed as follows:

$$\min G(\boldsymbol{x}) = (g_1(\boldsymbol{x}), g_2(\boldsymbol{x}), \cdots, g_N(\boldsymbol{x}))^{\mathrm{T}}$$
$$\boldsymbol{x} = (x_1, x_2, \cdots, x_m) \tag{5}$$

$$h_i(\boldsymbol{x}) \geq 0, \quad i = 1, 2, \cdots, p \tag{6}$$

where $\boldsymbol{x}$ is the decision vector composed of k design variables, $G(\boldsymbol{x})$ is the objective vector consisting of N objective functions $g_i(\boldsymbol{x})$, and $h_i(\boldsymbol{x})$ represents the inequality constraint function.

In multi-objective optimization, different objectives are usually coupled and constrained by the decision variables in the design space. Such problems generally yield a set of Pareto-optimal solutions. NSGA-II algorithm[35] reduces the computational complexity of non-dominated sorting by using a fast non-dominated sorting strategy. Its elitist strategy preserves high-quality individuals during evolution, thereby improving optimization accuracy and robustness.

The entropy weight method[36] was employed to evaluate and select the preferred solution from the Pareto front. This method determines objective weights based on the degree of data dispersion, thereby minimizing subjective bias in decision-making. First, the positive and negative indicators are normalized:

$$y_{ij} = \begin{cases} \dfrac{x_{ij} - \min(x_{ij})}{\max(x_{ij}) - \min(x_{ij})} \\ \\ \dfrac{\min(x_{ij}) - x_{ij}}{\max(x_{ij}) - \min(x_{ij})} \end{cases} \tag{7}$$

Then, the proportion p_{ij}, information entropy e_j, difference coefficient d_j, and entropy weight w_j of each indicator are calculated:

$$p_{ij} = \frac{y_{ij}}{\sum_{i=1}^{N} y_{ij}} \tag{8}$$

$$\begin{cases} e_j = -k \sum_{i=1}^{N} p_{ij} \ln(p_{ij}) \\ k = \dfrac{1}{\ln(N)} \end{cases} \quad \begin{cases} d_j = 1 - e_j \\ w_j = \dfrac{d_j}{\sum_{1}^{M} d_j} \end{cases} \tag{9}$$

An indicator with a greater degree of dispersion and lower information entropy receives a higher

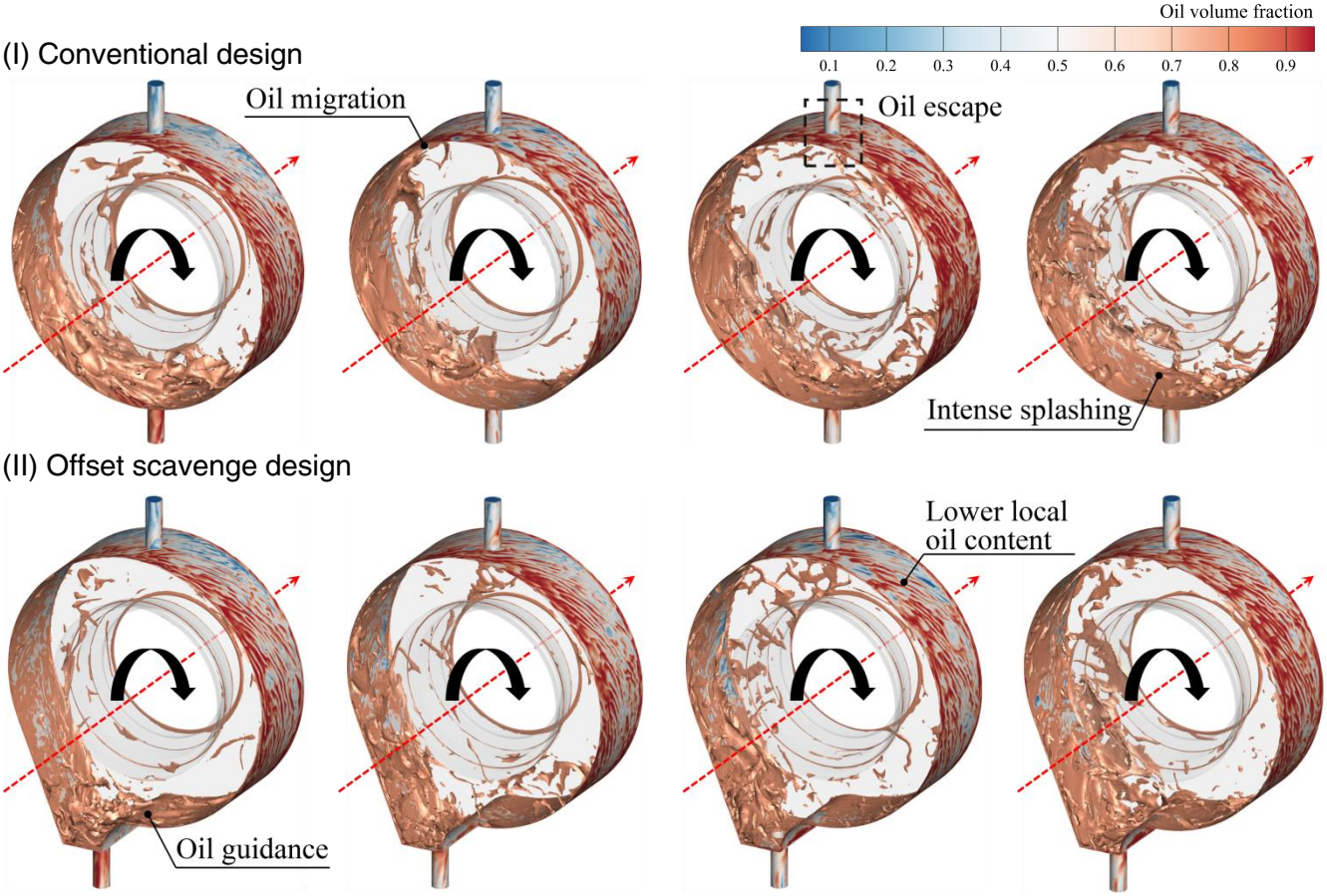
weight in the comprehensive evaluation. Once the weights are determined, the comprehensive evaluation score S_i for each scheme is calculated by weighted summation:

$$S_i = \sum_{j=1}^{M} w_j y_{ij} \tag{10}$$

3. Results and Discussion

3.1 Effect of rotational speed on scavenging and heat transfer

Figure 6 compares the oil phase distribution between the conventional and offset scavenge structures at various rotational speeds of q_{oil}=4 L/min, T_{oil}=423.15 K, q_{air}=1.5 g/s. In the conventional bearing chamber, the oil primarily migrates circumferentially along the chamber wall, resulting in extensive oil film coverage. As the rotational speed increases, oil splashing and breakup become more pronounced, with some oil migrating toward the vent region, indicating a tendency for oil escape. In contrast, the offset scavenge structure directs the oil toward the scavenge groove. The local oil content on the chamber wall is significantly reduced, and the oil distribution becomes more concentrated. This suggests that the offset scavenge structure improves the oil transport path and reduces ineffective oil retention within the chamber.

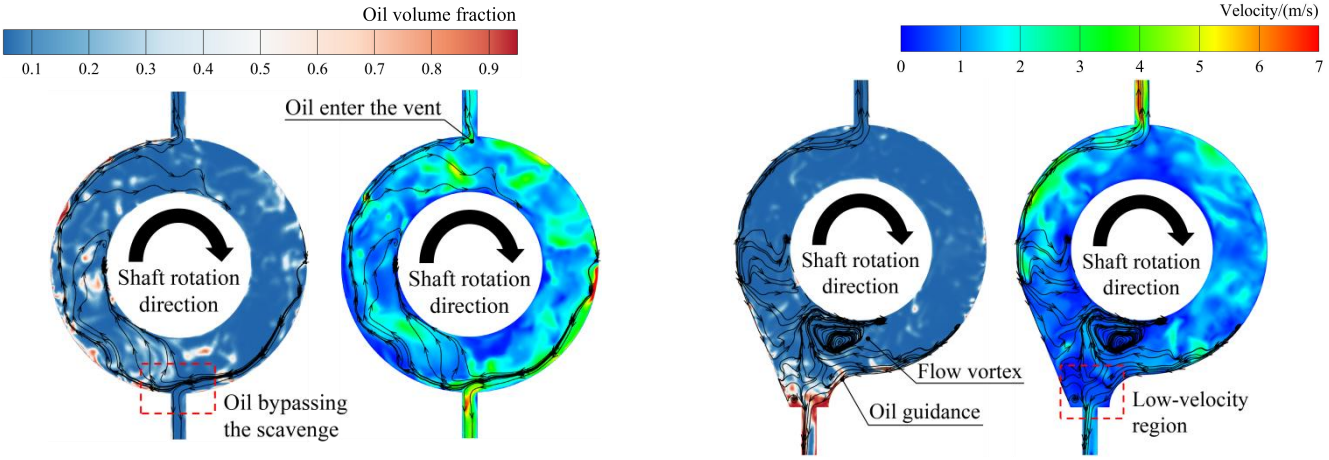


(a) 12000r/min (b) 14000r/min (c) 16000r/min (d) 18000r/min

Figure 6–Effect of n on oil distributions (q_{oil}=4 L/min, T_{oil}=423.15 K, q_{air}=1.5 g/s)

Figure 7 further illustrates the oil phase distribution, velocity contours, and streamlines for the two structures at design point. In the conventional structure, some oil bypasses the bottom scavenge outlet, continuing to flow along the wall or even migrating toward the vent region, resulting in oil scavenging loss. In contrast, the offset scavenge structure creates a distinct low-velocity region near the scavenge groove, where the oil is guided and collected toward the scavenge outlet. The streamline results

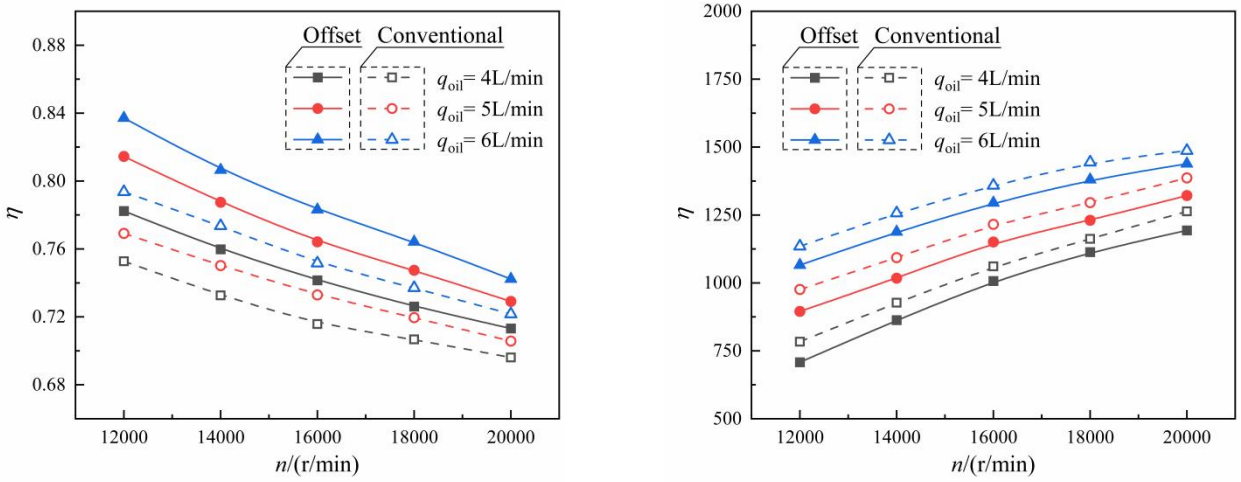
indicate that the offset structure provides a clearer oil discharge path, thereby enhancing the oil scavenging capability of the bearing chamber.



(a) Conventional design (b) Offset scavenge design

Figure 7–Comparison of flow field in different design

Figure 8 quantitatively compares the oil scavenging efficiency and the wall-averaged Nusselt number of the two structures at various rotational speeds and oil supply rates. As shown in Figure 8(a), the oil scavenging efficiency decreases with increasing rotational speed. This decline is primarily due to higher rotational speeds enhancing oil splashing and circumferential migration, which make it more difficult for some of the oil to be captured by the scavenge outlet. Conversely, increasing the oil supply rate improves the oil scavenging efficiency, as more oil is transported toward the lower part of the chamber. Compared to the conventional structure, within the rotational speed range of 12000–20000 r/min, the offset scavenge structure achieves an average improvement of 3.82% in oil scavenging efficiency under different oil supply rates, confirming its oil-guiding effect. Figure 8(b) shows the variation of the wall-averaged Nusselt number under different rotational speeds and oil supply rates. The Nusselt number increases with both rotational speed and oil supply rate. A higher rotational speed intensifies near-wall shear and enhances oil-air interaction, while a greater oil supply increases liquid film coverage on the chamber wall. Both factors promote convective heat transfer.



(a) Variation in η (b) Variation in Nu

Figure 8–Effect of n on scavenging and heat transfer

However, the offset scavenge structure results in a lower Nusselt number compared to the conventional structure. Within the rotational speed range of 12000–20000 r/min, the wall-averaged Nusselt number decreases by an average of 5.93% across different oil supply rates. This reduction is

primarily because the offset scavenge structure directs more oil toward the scavenge groove, reducing oil retention and local liquid film coverage on the wall. Consequently, the liquid-wall thermal coupling is weakened, leading to a lower level of wall heat transfer. Therefore, while the offset scavenge structure improves oil evacuation, it reduces wall heat transfer to some extent, indicating a trade-off between scavenging efficiency and heat transfer performance.

3.2 Effect of oil supply rate on scavenging and heat transfer

Figure 9 compares the oil phase distribution between the conventional and offset scavenge structures at various oil supply rates. In the conventional bearing chamber, the oil content increases significantly as the oil supply rate rises. The oil film coverage on the wall gradually expands, particularly near the scavenge outlet and the lower wall region, where more pronounced oil accumulation is observed. Additionally, the increased oil supply introduces more liquid into the chamber. Under the shear forces generated by the rotating airflow, local oil splashing and breakup become more intense, causing some of the oil to spread circumferentially and toward the upper region.

In contrast, the offset scavenge structure demonstrates a distinct oil-guiding effect across various oil supply rates. The oil is more effectively directed along the offset wall toward the scavenge groove, accumulating near the scavenge outlet. As the oil supply rate increases, oil retention near the scavenge groove also rises. However, the oil content in the upper chamber and areas distant from the scavenge outlet remains relatively low, indicating that the offset structure effectively limits large-scale oil dispersion within the chamber. Overall, increasing the oil supply rate enhances oil retention and wall coverage, and its interaction with airflow shear further promotes oil splashing to some extent.

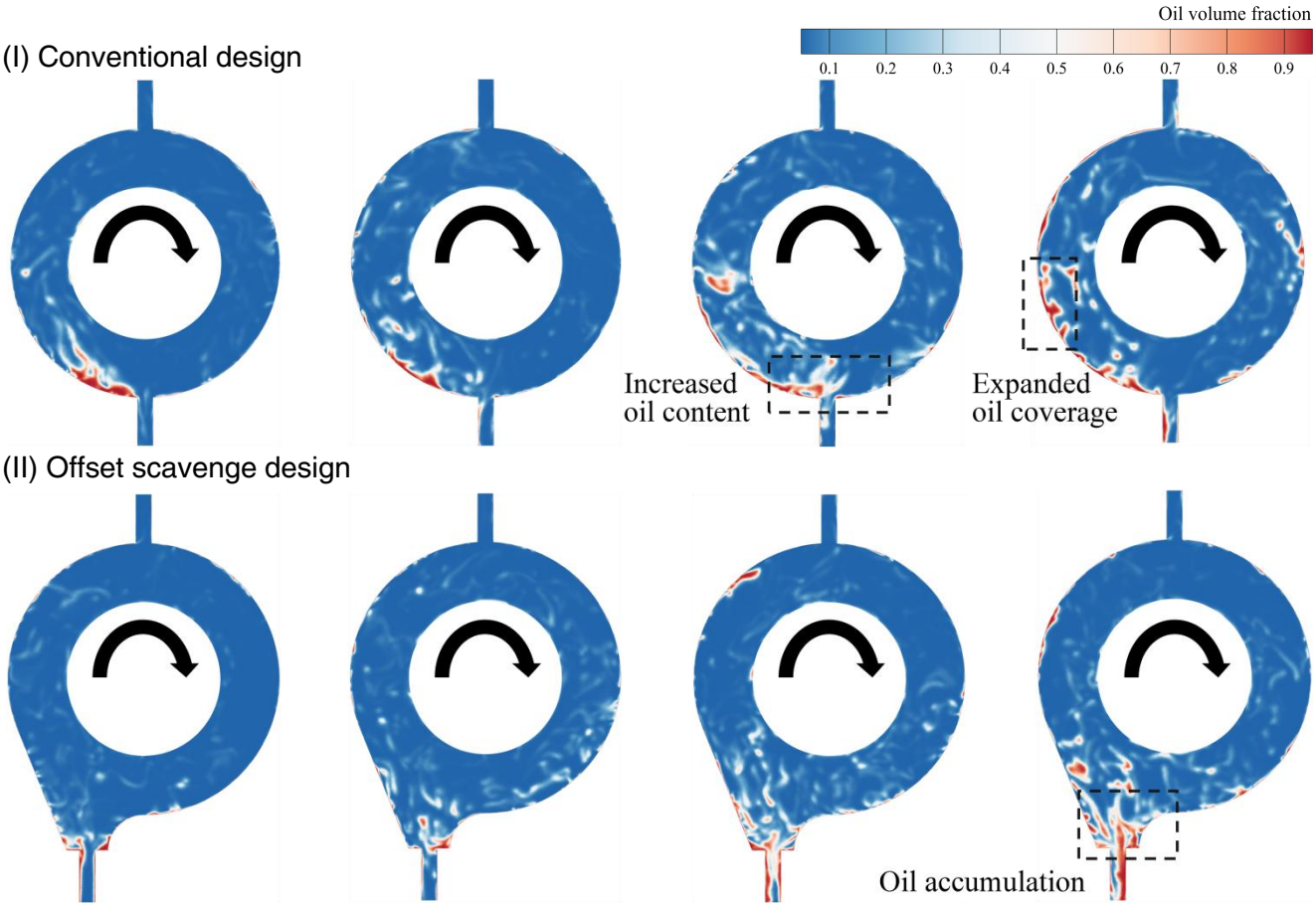
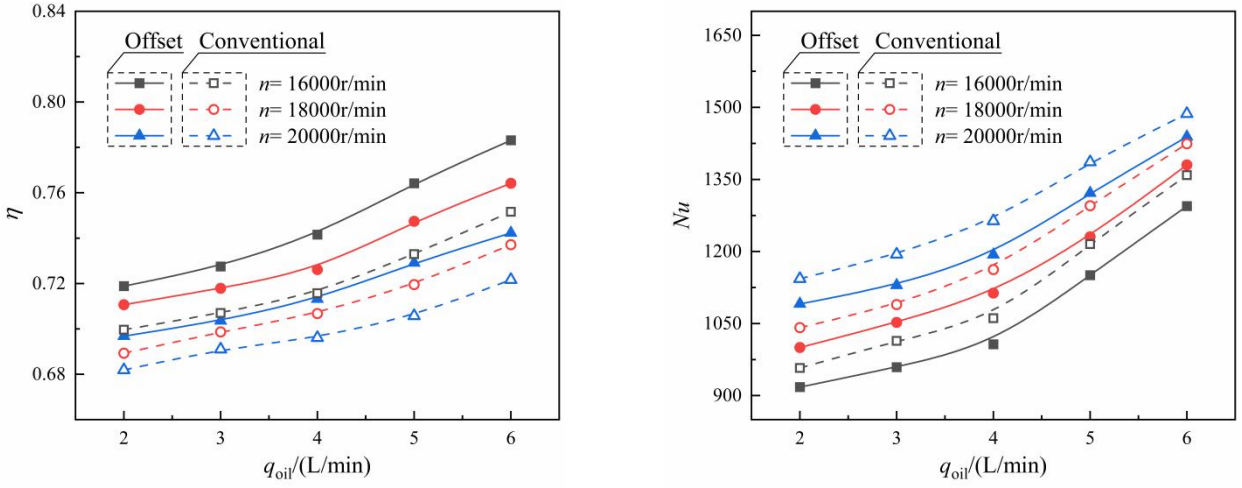


Figure 9–Effect of q_{oil} on oil distributions (n=16000 r/min, T_{oil}=423.15 K, q_{air}=1.5 g/s)

Figure 10 presents the quantitative variation in oil scavenging efficiency and the wall-averaged Nusselt number with oil supply rate. As q_{oil} increases from 2 L/min to 6 L/min, both structures exhibit an increase in scavenging efficiency. A higher oil supply rate delivers more oil to the lower part of the chamber, enabling the scavenge outlet to capture a greater amount of oil. Compared to the conventional structure, the offset scavenge structure maintains higher scavenging efficiency across the entire range of oil supply rates, indicating that its guiding effect remains effective under varying oil supply conditions.

The wall-averaged Nusselt number also increases with the oil supply rate. This increase is primarily due to the expanded oil coverage on the wall, as shown in Figure 9. With more liquid in contact with the heated surface, wall heat transfer is enhanced. However, the conventional structure generally produces a higher Nusselt number because more oil is distributed along the chamber wall. In contrast, in the offset scavenge structure, oil is more readily collected into the scavenge groove, resulting in lower local wall oil coverage and a relatively lower Nusselt number.



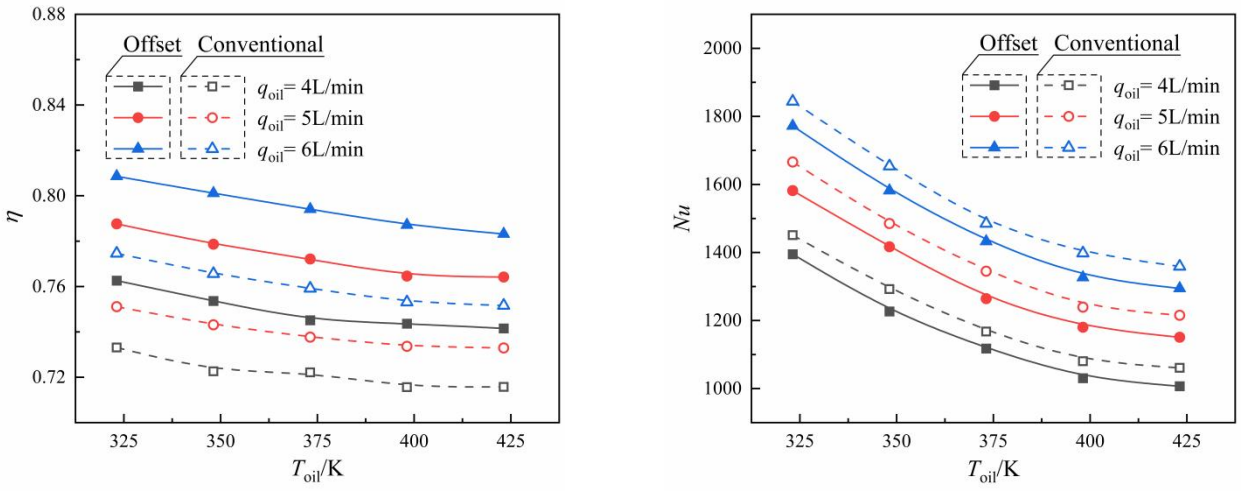
(a) Variation in η (b) Variation in Nu

Figure 10–Effect of q_{oil} on scavenging and heat transfer

3.3 Effect of oil supply temperature on scavenging and heat transfer

Figure 11 illustrates the effect of oil supply temperature. As T_{oil} increases from 323.15 K to 423.15 K, the oil scavenging efficiency of both structures decreases. Across different oil supply rates, the average decrease in scavenging efficiency is 2.74%. This reduction is mainly due to the decrease in oil viscosity at higher temperatures. The lower viscosity enhances oil mobility, making it easier for the oil to migrate along the chamber wall and escape through the vent, which leads to reduced scavenging efficiency.

The wall-averaged Nusselt number decreases significantly as the oil supply temperature increases. Across different oil supply rates, the average reduction in the Nusselt number reaches 27.04%. This decline is primarily due to the higher oil inlet temperature reducing the temperature difference between the oil phase and the heated wall, thereby diminishing the driving force for convective heat transfer. The offset scavenge structure continues to exhibit higher scavenging efficiency but a lower Nusselt number compared to the conventional structure, consistent with previous findings.



(a) Variation in η (b) Variation in Nu

Figure 11–Effect of T_{oil} on scavenging and heat transfer

3.4 Structure optimization and scheme decision-making

Overall, the offset scavenge structure enhances oil evacuation by directing oil toward the scavenge groove; however, the reduced wall oil coverage results in a lower wall-averaged Nusselt number. This indicates a trade-off between oil scavenging efficiency and heat transfer performance. Since both metrics are influenced by operating parameters, a simple parameter comparison is insufficient to identify the optimal design. Therefore, a multi-objective optimization method is introduced to improve the overall performance of the offset scavenge structure.

The structural parameters within the design space were sampled using the Latin Hypercube Sampling (LHS) method, resulting in 120 sample points. CFD simulations were then conducted on these samples to generate the corresponding performance responses. Based on the simulation data, a backpropagation (BP) neural network surrogate model was developed, with 80% of the samples used for training and the remaining 20% for testing. The network architecture was configured as 4-10-8-2, the learning rate was set to 0.0015, the maximum number of training epochs was 1500, and the target error was 1×10^{-5}. Five-fold cross-validation was performed to evaluate prediction accuracy. The average coefficient of determination (R^2) values for oil scavenging efficiency and wall-averaged Nusselt number were 0.992 and 0.994, respectively, with corresponding relative errors of 1.42% and 1.28%. These results indicate that the surrogate model exhibits high prediction accuracy and is suitable for subsequent optimization.

A well-designed bearing chamber should enhance oil scavenging efficiency while maintaining effective heat transfer performance, thereby reducing oil retention and lowering the chamber temperature. Consequently, maximizing oil scavenging efficiency and the wall-averaged Nusselt number were selected as the optimization objectives. The objective function was formulated as shown in Equation (11). The NSGA-II algorithm was employed for multi-objective optimization. The initial population size was set to 150, the number of generations to 80, the crossover probability to 0.9, and the mutation probability to 0.08.

$$\begin{cases} \max G(\boldsymbol{x}) = (g_1(\boldsymbol{x}), g_2(\boldsymbol{x}))^{\mathrm{T}} \\ g_1(\boldsymbol{x}) = \eta \\ g_2(\boldsymbol{x}) = Nu \end{cases} \quad \text{s.t.} \begin{cases} 24 \le w \le 64 \\ 15 \le h \le 35 \\ 10 \le d_s \le 18 \\ 10 \le d_v \le 18 \end{cases} \tag{11}$$

Figure 12 shows the optimal solution set obtained under the design-point condition. The Pareto

front is continuous and uniformly distributed, indicating that NSGA-II can effectively explore the objective space. Compared with the initial design (η=0.742, Nu=1006.92), the optimized Pareto front expands outward overall, with significant improvements in both objectives. The Pareto-optimal solutions were further evaluated using the entropy weight method. According to Equations (7)–(10), the weights of η and Nu were calculated as 0.586 and 0.413, respectively. After decision scoring of the Pareto front, the preferred design was selected, as shown in Table 2, and further validated through CFD simulation. The results indicate that the oil scavenging efficiency increased from 0.742 to 0.801 after optimization, representing an improvement of 7.96%. The Nusselt number rose from 1006.92 to 1049.42, reflecting a 4.22% increase. Additionally, the relative errors between the preferred design predicted by the surrogate model and the CFD validation results remain within 2%, further confirming the reliability of the optimization results.

It should be noted that the preferred scheme was selected based on the simultaneous improvement of oil scavenging efficiency and the Nusselt number compared to the original configuration. Therefore, the chosen solution is located within the dashed region in Figure 11. However, in practical applications, the final design can still be selected from the Pareto front according to specific requirements. For example, if oil scavenging efficiency is prioritized, a certain reduction in heat transfer performance may be acceptable, provided the wall temperature remains within the allowable range. Since the entropy weight method relies on the distribution of sample data, it cannot fully capture all practical constraints and system-level coupling effects. Therefore, the optimized design must still be evaluated in conjunction with overall characteristics of the lubrication system. Future work will incorporate system-level constraints to develop a more practical, multidimensional optimization framework.

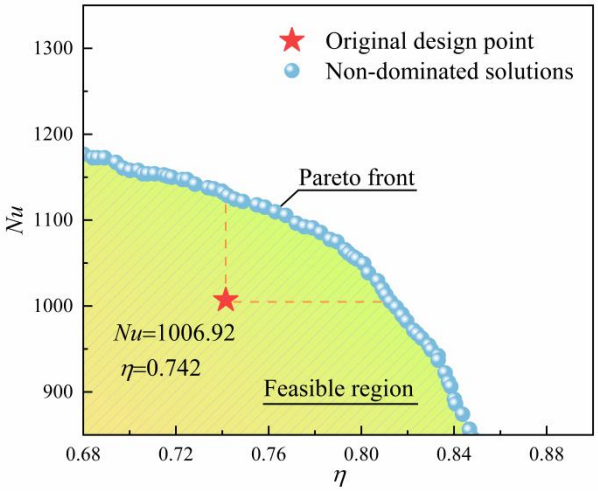


Figure 12–Pareto front of the multi-objective optimization

Table 2 Optimization scheme and results

Scheme	Parameters/mm				η	Nu
	h	w	d_v	d_s		
Original	25.0	35.0	11.5	11.5	0.742	1006.92
Optimization	30.2	58.1	14.5	16.8	0.801↑	1049.42↑

4. Conclusions

This study investigates the oil scavenging and heat transfer performance of an offset scavenge bearing chamber, and conducts multi-objective optimization using the NSGA-II algorithm. The main conclusions are as follows:

(1) Compared to the conventional design, the offset scavenge structure effectively directs oil toward the scavenge groove, thereby enhancing oil scavenging efficiency. However, the improved oil evacuation reduces the coverage of the wall oil film, resulting in a lower wall-averaged Nusselt number. This indicates a trade-off between oil scavenging efficiency and heat transfer performance.

(2) Operating parameters significantly affect the oil scavenging efficiency and heat transfer performance of the offset scavenge bearing chamber. Increasing the rotational speed enhances oil splashing and circumferential migration, which reduces oil scavenging efficiency but increases the wall-averaged Nusselt number. Increasing the oil supply rate improves wall oil film coverage, thereby enhancing both oil scavenging efficiency and Nusselt number. The oil supply temperature has a greater impact on heat transfer performance than on scavenging efficiency. As the oil supply temperature rises from 323.15 K to 423.15 K, the oil scavenging efficiency decreases by an average of 2.74%, while the wall-averaged Nusselt number decreases by 27.04%.

(3) The NSGA-II-based multi-objective optimization framework effectively enhances the performance of the offset scavenge bearing chamber. Compared to the initial design, the optimized structure increases oil scavenging efficiency by 7.96% and the Nusselt number by 4.22%. This optimization method offers a valuable reference for lubrication system design and thermal management.

5. Contact Author Email Address

Yaguo Lyu: yglu@nwpu.edu.cn

6. Copyright Statement

The authors confirm that they, and/or their company or organization, hold copyright on all of the original material included in this paper. The authors also confirm that they have obtained permission, from the copyright holder of any third party material included in this paper, to publish it as part of their paper. The authors confirm that they give permission, or have obtained permission from the copyright holder of this paper, for the publication and distribution of this paper as part of the ICAS proceedings or as individual off-prints from the proceedings.

References

[1] He B, Yuan X, Qian S, et al. Carbon neutrality: a review. Journal of Computing and Information Science in Engineering, 2023, 23(6): 060809.

[2] Zhu Z, Lyu Y, Jiang L, et al. Two-phase flow characteristics in dual-rotor support bearing chamber of aero-engines and sensitivity analysis. *Thermal Science and Engineering Progress*, 2026: 104675.

[3] Li R, Zhu P, Yuan H, et al. Dynamics of oil droplet impacting oil film in bearing chamber. *International Journal of Mechanical Sciences*, 2025, 302: 110555.

[4] Li Y, Jiang L, Chen Y, et al. Performance analysis of boosted centrifugal separators and matching characteristics with ventilation systems in aero-engine. *Aerospace Science and Technology*, 2026: 111715.

[5] Jiang L, Liu Z, Huang W, et al. Numerical and experimental investigation on two-phase flow and oil capture efficiency of under-race lubrication for high-speed bearings. *Physics of Fluids*, 2024, 36(6).

[6] Lee C W, Palma P C, Simmons K, et al. Comparison of computational fluid dynamics and particle image velocimetry data for the airflow in an aeroengine bearing chamber. *Journal of Engineering for Gas Turbines and Power*, 2005, 127(4): 697-703.

[7] Aidarinis J, Missirlis D, Yakinthos K, et al. CFD modeling and LDA measurements for the air-flow in an aero engine front bearing chamber. *Journal of Engineering for Gas Turbines and Power*, 2011.

[8] Glahn A, Wittig S. Two-phase air/oil flow in aero engine bearing chambers: characterization of oil film flows. *Journal of Engineering for Gas Turbines and Power*, 1996, 118(3): 578-583.

[9] Glahn A, Blair M F, Allard K L, et al. Disintegration of oil films emerging from radial holes in a rotating cylinder. *J. Eng. Gas Turbines Power*, 2003, 125(4): 1011-1020.

[10] Farrall M, Simmons K, Hibberd S, et al. A numerical model for oil film flow in an aeroengine bearing chamber and comparison to experimental data. *Journal of Engineering for Gas Turbines and Power*, 2006, 128(1): 111-117.

[11] Zhu D , Chen G D, Wang L, et al. Effects of droplet deformation, evaporation, and mutual interaction with air on droplet motion and droplet-film impingement in aeroengine bearing chambers. *Applied Thermal Engineering*, 2023; 224: 120008.

[12] Singh K, Sharabi M, Jefferson R, et al. Modelling of partially wetting liquid film using an enhanced thin film model for aero-engine bearing chamber applications. *ASME Turbo Expo 2020: Turbomachinery Technical Conference and Exposition*, 2020: 15845.

[13] Simmons K, Hibberd S, Wang Y, et al. Numerical study of the two-phase air/oil flow within an aero-engine bearing chamber model using a coupled Lagrangian droplet tracking method. *ASME Pressure Vessels and Piping Conference*. 2002, 46598: 325-331.

[14] Young C, Chew J W. Evaluation of the volume of fluid modelling approach for simulation of oil/air system flows. *ASME Turbo Expo: Power for Land, Sea, and Air*. 2005, 47268: 1249-1257.

[15] Kirov N K, Zuzio D, Senoner J M, et al. Assessment of Multi-Fluid, Eulerian integral thin film and DPM approaches for the numerical simulation of a bearing chamber. *Multiphase Science and Technology*. 2024; 36: 49-68.

[16] Kurz W, Bauer H J. An approach for predicting the flow regime in an aero engine bearing chamber. *Turbo Expo: Power for Land, Sea, and Air. American Society of Mechanical Engineers*, 2014, 45738: V05CT16A037.

[17] Yuan X C, Guo H, Wang L Y. Experiment study of heat transfer in aeroengine bearing chambers. *Applied Mechanics and Materials*, 2011, 86: 448-453.

[18] Wittig S, Glahn A, Himmelsbach J. Influence of high rotational speeds on heat transfer and oil film thickness in aero-engine bearing chambers. *Journal of Engineering for Gas Turbines and Power*. 1994, 116(2): 395-40.

[19] Glahn A, Wittig S. Two-phase air/oil flow in aero-engine bearing chambers-assessment of an analytical prediction method for the internal wall heat transfer. *International Journal of Rotating Machinery*, 1999, 5(3): 155-165.

[20] Busam Stefan, Glahn Axel, Wittig Sigmar. Internal bearing chamber wall heat transfer as a function of operating conditions and chamber geometry. *Journal of Engineering for Gas Turbines and Power*. 2000, 122(2): 314-320.

[21] Petukhov I, Kovalov A, Mykhailenko T. Mathematical modelling of heat transfer in air-droplet flow of GTE bearing chamber. *Aerospace Technic and Technology*, 2022 (6): 23-30.

[22] Tatar V, Piskin A. Numerical investigation on bearing chamber wall heat transfer. *Turbo Expo: Power for Land, Sea, and Air. American Society of Mechanical Engineers*, 2018, 50985: V001T01A014.

[23] Chandra B, Simmons K, Pickering S, et al. Factors affecting oil removal from an aeroengine bearing chamber. *Turbo Expo: Power for Land, Sea, and Air*. 2010, 43963: 219-228.

[24] Chandra B, Simmons K, Pickering S, et al. Study of gas/liquid behavior within an aeroengine bearing chamber. *Journal of engineering for gas turbines and power*, 2013, 135(5): 051201.

[25] Chandra B W, Collicott S H, Munson J H. Experimental optimization of rolls-royce ae3007 sump design. *Turbo Expo: Power for Land, Sea, and Air. American Society of Mechanical Engineers*, 2017, 50770: V001T01A022.

[26] Adeniyi A A, Chandra B, Simmons K. Computational study of a customised shallow-sump aero-engine bearing chamber with inserts to improve oil residence volume. *Turbo Expo: Power for Land, Sea, and Air. American Society of Mechanical Engineers*, 2017, 50886: V05BT15A022.

[27] Wolfram Kurz, Klaus Dullenkopf, Hans-Jorg Bauer. Capacitive film thickness measurements in a ventless aero-engine bearing chamber: Influence of operating conditions and offtake design. *Journal of Engineering for Gas Turbines and Power*. 2013, 135(112504): 1-7.

[28] Niu Y, Zhao K, Yao M, et al. Aerodynamic force prediction of compressor blade surfaces based on machine learning. *Physics of Fluids*, 2024, 36(8).

[29] Wu Y, Ba D, Du J, et al. Fast prediction of compressor flow field based on a deep attention symmetrical neural network. *Physics of Fluids*, 2024, 36(11).

[30] Yan H, Ye L, Zhou T L, et al. Physics-informed neural network for predicting multi-row film cooling superposition using Fourier transform and attention mechanism. *Physics of Fluids*, 2025, 37(6).

[31] Fan P, Kong X, Huang T, et al. Optimization design of seal cavities for shrouded stators. *Physics of Fluids*, 2024, 36(11).

[32] Krug M B, Höfler C, Bauer H, Et Al. Evaluation of the volume-of-fluid method for the numerical modelling of an aero engine bearing chamber. *The 22nd International Symposium on Air Breathing Engines*. 2015: 1-10.

[33] Hirt C W, Nichols B D. Volume of fluid (VOF) method for the dynamics of free boundaries. *Journal of Computational Physics*, 1981, 39(1): 201-225.

[34] Menter F R. Two-equation eddy-viscosity turbulence models for engineering applications. *AIAA journal*, 1994, 32(8): 1598-1605.

[35] Deb K, Pratap A, Agarwal S, et al. A fast and elitist multiobjective genetic algorithm: NSGA-II. *IEEE transactions on evolutionary computation*, 2002, 6(2): 182-197.

[36] Huang J. Combining entropy weight and TOPSIS method for information system selection. *2008 IEEE conference on cybernetics and intelligent systems*, 2008: 1281-1284.